

HDR Imaging with Quanta Image Sensors: Theoretical Limits and Optimal Reconstruction

Abhiram Gnanasambandam, *Student Member, IEEE*, and Stanley H. Chan, *Senior Member, IEEE*

Abstract—High dynamic range (HDR) imaging is one of the biggest achievements in modern photography. Traditional solutions to HDR imaging are designed for and applied to CMOS image sensors (CIS). However, the mainstream one-micron CIS cameras today generally have a high read noise and low frame-rate. These, in turn, limit the acquisition speed and quality, making the cameras slow in the HDR mode. In this paper, we propose a new computational photography technique for HDR imaging. Recognizing the limitations of CIS, we use the Quanta Image Sensor (QIS) to trade the spatial-temporal resolution with bit-depth. QIS is a single-photon image sensor that has comparable pixel pitch to CIS but substantially lower dark current and read noise. We provide a complete theoretical characterization of the sensor in the context of HDR imaging, by proving the fundamental limits in the dynamic range that QIS can offer and the trade-offs with noise and speed. In addition, we derive an optimal reconstruction algorithm for single-bit and multi-bit QIS. Our algorithm is theoretically optimal for all linear reconstruction schemes based on exposure bracketing. Experimental results confirm the validity of the theory and algorithm, based on synthetic and real QIS data.

Index Terms—Quanta Image Sensors, High Dynamic Range, Signal-To-Noise Ratio, Photon Counting

I. INTRODUCTION

Quanta image sensors (QIS) are a new type of image sensors with single photon sensitivity. Originally proposed in 2005, the sensor was designed to overcome the full-well capacity limit of the mainstream CMOS image sensors (CIS) due to the shrinking pixel sizes [1], [2]. Compared to CIS, the anticipated QIS will have a smaller pixel pitch, higher frame rate, smaller read noise, and dark current. As recently reported in [3], the latest QIS prototype has achieved a read noise below $0.25e^-$ rms at room temperature and a frame rate beyond 1000 frames per second, while the pixel pitch is only $1.1\mu\text{m}$. The small pixel pitch of the sensors allows higher spatial resolution per unit area. The small read noise and dark current also allow the sensors to perform single photon counting at room temperature. Besides, the fabrication of QIS is based on the standard 3D stacking techniques widely used for CIS [3], and hence the potential cost of QIS can be comparable to a CIS. These factors have made QIS an excellent candidate for imaging dark and dynamic scenes. Recent reports in computer vision have proved the effectiveness of the sensors in various applications [4]–[7].

A. Current state-of-the-art HDR imaging

High dynamic range (HDR) imaging refers to capturing an image where the photon flux varies substantially between different parts of the image. Without a customized acquisition scheme and reconstruction technique, pixels of a HDR scene will saturate in the bright regions whereas pixels in dark regions will not have enough photons. In either case, the signal to noise ratio will be poor. The goal of HDR imaging is to capture the scene such that we can maintain a consistent signal-to-noise ratio (SNR) throughout the image.

HDR imaging is ubiquitous in photography, microscopy, navigation, and surveillance, to just name a few. We refer the readers to the texts by Banterle et al. [8] and Reinhard et al. [9] for an introduction to the subject. In general, HDR imaging techniques can be categorized into three families: (i) exposure bracketing [10]–[14], (ii) coded exposure [15], [16], and (iii) burst photography [17]–[19].

CIS-based exposure bracketing. In exposure bracketing, we take multiple exposures of the scene, some with longer and some with shorter exposures, then use a carefully designed image processing algorithm to merge these differently exposed images to form the final image. Exposure bracketing is popular because of the simplicity which allows it to be used on hand-held devices. The downside, however, is that it requires capturing many long and short exposure frames before the fusion step. The overall acquisition time is thus long.

Despite the great variety of exposure bracketing techniques, one thing that remains unchanged is the original linear combination idea. There are multiple ways of achieving linear reconstruction. One can combine processed images instead of the raw image [10], [13], [20], or directly use the raw data [12], [21]–[23]. The choice of the combination weight also plays a critical role in HDR reconstruction. In [10], the weights are chosen to be proportional to the SNR so that the overall SNR of the combined image is optimized. [24] proposes two different ways to obtain an HDR image, either by maximizing the minimum SNR in the image or minimizing the overall time taken to obtain an image with a particular minimum SNR. In [21], Robertson et al. proved that the maximum likelihood estimate of the HDR estimate is the linear combination with weights inversely proportional to the variance of the signal. [12] extends the work of [21] by including different sources of noise in the model. [25] proposes to combine LDR images with just their pixel values without converting them into HDR values. Recently, several neural-network based HDR reconstruction methods that hallucinate HDR images from LDR images [26], [27] or use exposure

A. Gnanasambandam and S. Chan are with the School of Electrical and Computer Engineering, Purdue University, West Lafayette, IN 47907, USA. Email: agnanasa, stanchan@purdue.edu.

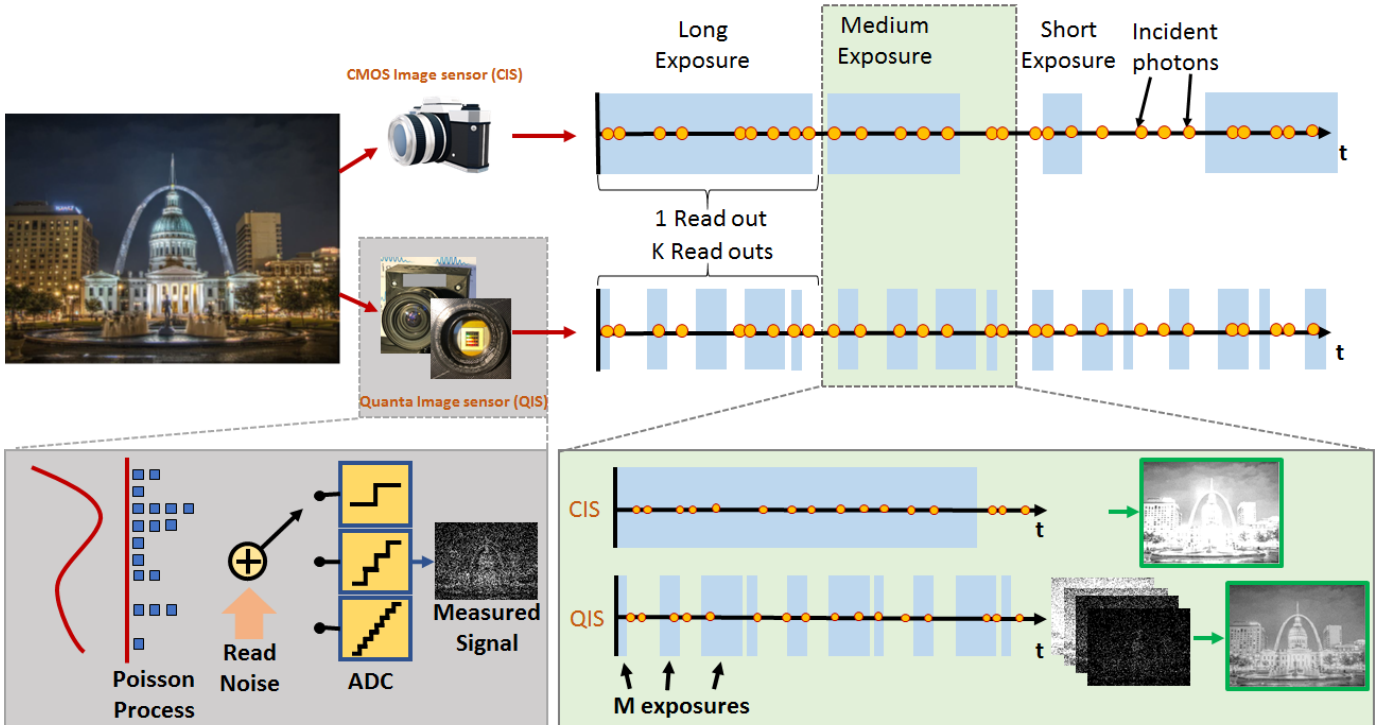


Fig. 1. **HDR Imaging with Quanta Image Sensors.** Quanta Image Sensors have the ability to oversample the scene, because of their significantly higher frame rate. In this paper, we show that when we combine the oversampling ability of Quanta Image Sensors with exposure bracketing, the dynamic range achieved by the system far exceeds the dynamic range of the CMOS Image Sensors.

bracketed images for reconstructing HDR dynamic scenes have also been proposed [28], [29].

CIS-based coded exposure. Coded exposure can be thought of as a modified version of exposure bracketing, where instead of capturing multiple frames with different exposures, we capture a single frame with different exposures, and use carefully developed algorithms to combine these different exposures into a single image. Some representative works include [16], which proposed using spatially varying exposures to obtain HDR imaging in a single frame, and [15] which extended the idea by using convolutional sparse coding.

CIS-based burst photography. The idea of burst photography is to acquire a burst of short exposure frames so that all the frames are below the saturation limit. Then, by properly aligning the images (with respect to object motion and camera motion), one can reconstruct an HDR image. Over the past few years, various burst photography algorithms are proposed, ranging from the more traditional motion alignment methods [30]–[32] to the more recent end-to-end deep learning methods [33]–[35]. However, CIS-based burst photography is intrinsically limited by the photon sensitivity of the sensors. As the exposure becomes increasingly short, the high read noise and dark current of the sensor will prohibit the precise measurement of the signals. This, when added to the random Poisson statistics of the photon arrivals, poses a fundamental limit to CIS-based burst photography which cannot be solved by pure image processing, including deep learning algorithms.

B. Quanta Image Sensors

Being a single-photon image sensor, QIS have substantially better photon sensitivity than CIS. This unique capability opens the door to a new way of acquiring HDR images. In particular, with QIS one can operate in a regime that allows significantly shorter exposure and higher frame rate while still being able to resolve the incoming photons. CIS-based techniques are harder to operate in this regime because as the exposures become short, the read noise and dark current of the sensor will wash out the detectable signals.

Image reconstruction for Quanta Image Sensors. In recent years, there have been a large number of works on image reconstruction for QIS [4], [7], [36]–[38]. Using QIS for better HDR imaging has been hypothesized for several years [39]. For single-bit QIS, Yang et al. [40] showed how oversampling can be theoretically beneficial for the dynamic range. One way to achieve the goal is to control the threshold dynamically, as proposed by Elgendy and Chan [41]. In this paper, instead of controlling the threshold we acquire multiple exposures and seek reconstruction.

C. HDR imaging using Quanta Image Sensors

We present in this paper a QIS based HDR imaging principle, as outlined in Figure 1. Within one CIS exposure, we use the QIS to over-sample the scene by taking multiple very short exposure frames of different integration periods. Depending on the full-well capacity and the scene dynamics,

we can manually control the QIS to output 1-bit signals or few-bit signals by adjusting the analog-to-digital converter (ADC) [39], [42]. The raw captures of the sensor are a stack of low bit-depth frames, some with longer exposures and some with shorter exposures. Because of the unique QIS statistics, we derive a customized image fusion algorithm to reconstruct an HDR image from the raw data.

There are several benefits of using QIS for HDR imaging compared to CIS. As we will theoretically derive in this paper, for the same total integration time, QIS offers a higher SNR compared to CIS. This, in turn, provides a wider dynamic range of the sensor. Besides, since QIS can capture multiple exposures within a short period, the overall acquisition time can be much shorter than that of CIS. For scenes containing moving objects, the short acquisition time of QIS is fundamentally more advantageous because it allows us to resolve the moving content while maintaining the dynamic range. Furthermore, by construction, the QIS has a much higher photon sensitivity than the CIS. Therefore, the QIS can handle low-light conditions much more effectively than the CIS.

D. Single-photon avalanche diodes

Single Photon Avalanche Diodes (SPAD) [43]–[45] is an alternative technology to the CMOS-based QIS we use in this paper. SPADs are different from QIS in multiple ways. First, they amplify signals using avalanche multiplication. As such, SPADs require higher operating voltages (15–20V). SPAD also have high dark current ($> 10e^-/\text{pix/s}$), large pitch ($> 5\mu\text{m}$), low fill-factor ($< 70\%$), and low quantum efficiency ($< 50\%$). In comparison, QIS do not use avalanche multiplication. It has smaller dark current ($< 0.1e^-/\text{pix/s}$), smaller pixel pitch ($1.1\mu\text{m}$), higher fill factor ($> 90\%$), and higher quantum efficiency ($> 70\%$). SPAD have better frame-rate (upto 97k frames/sec) compared to QIS (1040 frames/sec), because of which SPAD are better suited for applications such as time-of-flight imaging, where resolving time stamps of the photon arrival is needed.

Using SPAD for HDR imaging has recently been demonstrated in several papers. Dutton et al. [46] showed a new method to perform HDR imaging with active clock-driven SPAD image sensors using exposure bracketing. Ingle et al. [47] showed the suitability of active event-driven SPAD image sensors for passive HDR imaging. While SPADs have superior time resolving capability, QIS offer higher spatial resolution. QIS can capture multi-bit frames, but SPAD can operate only in a single-bit mode. The QIS we use in this paper is clock-driven, so it is comparable to the SPAD uses in [46]. However, [46] simply sums multiple frames to reconstruct an HDR image which is not optimal. The HDR reconstruction method we are developing could be applied to the SPADs with some modifications of the parameters such as read noise, dark current, and bit-depth.

E. Challenges and contributions

QIS is arguably a young technology. While previous work of Yang et al. [40], Fossum [39], [42], and Elgendy and Chan

[36], [41] have laid the mathematical foundations of the sensor’s sampling mechanisms and various image reconstruction algorithms, the sensor’s performance for HDR imaging has never been systematically studied. The two biggest questions are: (i) to what extent the dynamic range can be offered by the QIS, and (ii) by what reconstruction algorithm we need to use for QIS. The goal of this paper is to fill the gap by outlining the theoretical performance limits of the sensors (Section III), and propose a new image fusion algorithm to merge the raw QIS data into an HDR image (Section IV). By accomplishing this goal, we aim to provide an alternative HDR imaging approach.

The algorithmic contributions of this paper can be summarized in Figure 2. The input to the algorithm is a stack of images taken at different integration times. Assuming statistical independence of the measurements within the exposure stacks, previous work of Chan et al. [36] showed that the sum of the frames is a sufficient statistic of the scene. This allows us to create rough estimates of the low dynamic range (LDR) images. In this paper, we develop an iterative updating procedure to estimate the HDR image and predict the signal-to-noise ratio. The feedback loop continues until the algorithm converges. More specifically, we contribute to the literature of QIS and HDR imaging in the following ways:

- 1) We theoretically derive a closed-form expression for the signal-to-noise ratio (SNR) of QIS, with consideration of shot noise and read noise. We show that our theoretical prediction is close to the real data from a QIS camera.
- 2) We use the SNR expression derived to compare the dynamic range of the QIS with CIS, from which we demonstrate the cost-benefit of QIS for high dynamic range imaging.
- 3) We develop a provably optimal HDR reconstruction algorithm that linearly combines the low dynamic range images, whose weights are obtained using the SNR values of each pixel at different integration times.

The QIS camera we use in this paper is the *PathFinder* camera developed by Gigajot Technology Inc. and Dartmouth College. Since the camera is still a prototype, we acknowledge its non-ideal optics and circuits.

II. BACKGROUND

A. Imaging model of QIS

The principle of QIS is to partition a pixel into many tiny cells called jots where each jot is a single-photon image sensor. Because of the small pixel pitch and the fast response, QIS can be regarded as an *oversampling* device which oversamples the space and time. To understand how the sensors work, in this section we discuss their imaging model. Our model is more detailed than the previously studied models, e.g., [36], [40], [41], which focus mainly on the shot noise. We consider several other sources of noise. Table I shows a list of notations used in this paper.

Let $\lambda(t) = [\lambda_1(t), \dots, \lambda_d(t)]^T \in \mathbb{R}^d$ be an d -dimensional vector field representing the photon flux with d pixels located at time $t \in \mathbb{R}$. Let T be the duty cycle when acquiring an image, and define the integration time as $[nT, nT + \Delta]$, for

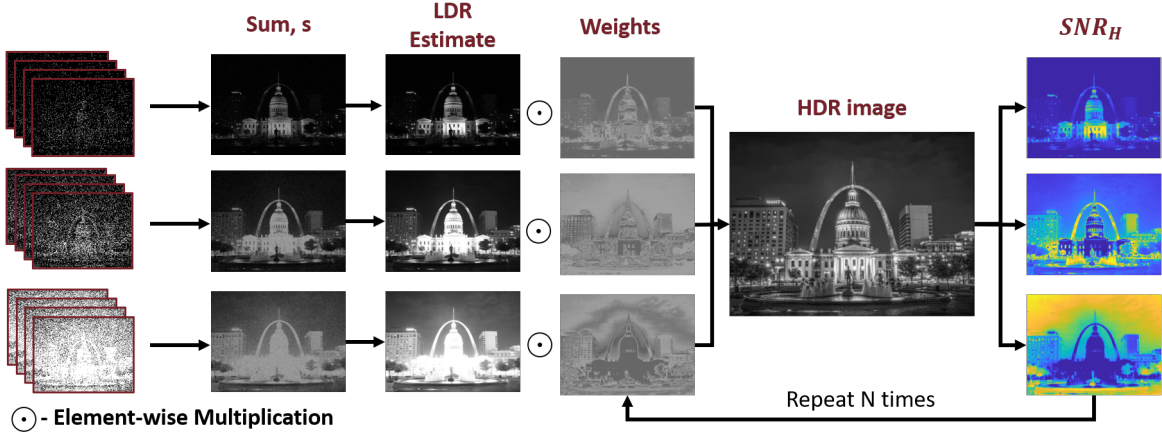


Fig. 2. **HDR Reconstruction Pipeline.** The raw frames from QIS are first summed and denoised. Then the denoised images are linearly combined by giving weights to each image proportional to their SNR_H iteratively. (See Section IV)

Symbols	Meanings
d	Number of pixels
λ	Photon flux from the scene
T	Duty cycle of the camera
Δ	Integration time
θ	Mean number of photons arriving at the sensor
μ_{dark}	Mean dark current
\mathbf{K}	Number of photons detected by the sensor
η_{red}	Read noise from the image sensor
σ_{red}	Variance of the read noise
\mathbf{Z}	Analog signal from the sensor
\mathbf{Y}	Digitized signal from the sensor
\mathcal{Y}	Set of frames obtained at different integration times
σ_H	Exposure-referred noise
SNR_H	Exposure-referred SNR
N	Total Number of frames collected
M	Number of different integration times
$\Psi_q(\cdot)$	Incomplete Gamma function

TABLE I

NOTATIONS USED IN THIS PAPER.

$n = 1, \dots, N$. The mean number of electrons excited by the photons at the sensor is

$$\theta[n] = \int_{nT}^{nT+\Delta} \lambda(\tau) d\tau. \quad (1)$$

The resulting vector field $\theta[n] = [\theta_1[n], \theta_2[n], \dots, \theta_d[n]]^T$, where $n = 1, 2, \dots, N$, can be regarded as a video sequence of d pixels and N frames.

Given $\theta[n]$, we model the photon arrival as a Poisson process. Letting $\mathbf{K}[n] = [K_1[n], \dots, K_d[n]]^T$ be the number of photons detected by the sensor, we model $\mathbf{K}[n]$ as

$$\underbrace{\mathbf{K}[n]}_{\text{number of photons}} \sim \underbrace{\text{Poisson}(\theta[n] + \mu_{\text{dark}})}_{\text{Poisson process}}, \quad (2)$$

where $\text{Poisson}(\cdot)$ denotes the Poisson distribution, and μ_{dark} is the average dark current.

During the read out, we model the read noise as an i.i.d. Gaussian random variable, i.e., $\eta_{\text{read}}[n] \sim \mathcal{N}(0, \sigma_{\text{read}}^2 \mathbf{I})$. This

leads to the signal $\mathbf{Z}[n] = [Z_1[n], \dots, Z_d[n]]^T$, where

$$\mathbf{Z}[n] = \underbrace{\mathbf{K}[n]}_{\text{number of photons}} + \underbrace{\eta_{\text{read}}[n]}_{\text{read noise}}. \quad (3)$$

Here, we denote the vector $\mathbf{Z}[n]$ in upper case to emphasize that it is a random vector. The distribution of $\mathbf{Z}[n]$ is Poisson-Gaussian. Specifically, letting $\vartheta_i = \theta_i[n] + \mu_{\text{dark}}$ be the Poisson mean, the probability of $Z_i[n] = z$ is given by

$$\mathbb{P}[Z_i[n] = z] = \sum_{\ell=0}^{\infty} \left(\frac{\vartheta_i^\ell}{\ell!} e^{-\vartheta_i} \cdot \frac{1}{\sqrt{2\pi\sigma_{\text{read}}^2}} e^{-\frac{(z-\ell)^2}{2\sigma_{\text{read}}^2}} \right). \quad (4)$$

Finally, to generate a digital signal, we convert the real number $\mathbf{Z}[n]$ using an analog-to-digital converter (ADC). Depending on the number of bits used by the ADC, we can operate the QIS in a single-bit mode or a multi-bit mode. For **single-bit**, the ADC binarizes the signal as

$$Y_i[n] \stackrel{\text{def}}{=} \text{ADC}(Z_i[n]) = \begin{cases} 1, & \text{if } Z_i[n] \geq L, \\ 0, & \text{if } Z_i[n] < L. \end{cases} \quad (5)$$

For **multi-bit**, the ADC returns

$$Y_i[n] \stackrel{\text{def}}{=} \text{ADC}(Z_i[n]) = \begin{cases} L, & [Z_i[n]] \geq L, \\ [Z_i[n]], & [Z_i[n]] < L, \end{cases} \quad (6)$$

where $[\cdot]$ is function that rounds off the real valued numbers to the nearest integer. The final raw QIS signal generated is therefore a sequence of vectors

$$\mathcal{Y} = \left\{ \underbrace{\mathbf{Y}[1], \dots, \mathbf{Y}[m]}_{\text{Exposure 1}} \dots \underbrace{\mathbf{Y}[n], \dots, \mathbf{Y}[N]}_{\text{Exposure M}} \right\}, \quad (7)$$

where each $\mathbf{Y}[n] = [Y_1[n], \dots, Y_d[n]]^T$. Our goal is to reconstruct $\theta[n]$ from \mathcal{Y} . For repeated measurements of the same scene, we will have multiple copies of \mathcal{Y} .

B. Model validation with real data

The model presented above is more comprehensive than the popular models in [36] and [40]. To validate our model we compare it with the real data collected by a prototype QIS

camera. The experiment was first reported in [48], and we repeat the experiment again in this paper for completeness.

In this experiment, we use a uniform illumination so that $\lambda[n]$ is a constant. A total of 50,000 repeated measurements from a single pixel is used to construct a photon counting histogram as shown in Figure 3. Each measurement has an integration time of $50\mu\text{s}$. The average photon count is 1.48 photons per pixel (ppp). The ADC uses a bit-depth of 14 bits. The least significant bit is $0.05e^-$. Because the ADC uses 14 bits, the resulting histogram is close to a continuum.

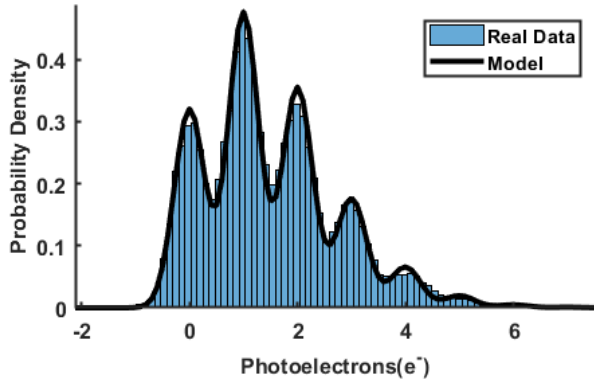


Fig. 3. **Validation of the Model.** First reported in [48]. We compute the photon counting histogram of a real QIS sensor and compare it with our theoretical model. Note the similarity between the two.

To plot the theoretical model, we assume that the read noise level is $0.25e^-$. The dark current is assumed to be $0.0068e^-$ per second. Now, once we know the scene intensity λ , we can plot the black curve. λ chosen such that the mean squared error between the histogram and the theoretical curve is minimized. However, since the integration time is only $50\mu\text{s}$, we can safely neglect the dark current. Putting these together we obtain the black curve as shown in Figure 3. As we can see, the theoretical model fits the real data well.

III. THEORETICAL ANALYSIS OF QIS DYNAMIC RANGE

In this section, we theoretically derive the dynamic range of a QIS. Figure 4 shows an illustration of the meaning of the dynamic range. In a nutshell, the dynamic range is the range of the exposure such that the signal-to-noise ratio (SNR) is above a certain threshold. Therefore, to analyze the dynamic range of QIS, we need to first define the SNR and then understand how the SNR will change when different sensor parameters change.

A. Signal to noise ratio (SNR)

To simplify our notation, we will focus on the i -th pixel $Y[n] = Y_i[n]$, for $n = 1, \dots, N$. Since the sensor response of QIS is a nonlinear, we follow [39] and [41] by considering the exposure-referred SNR.

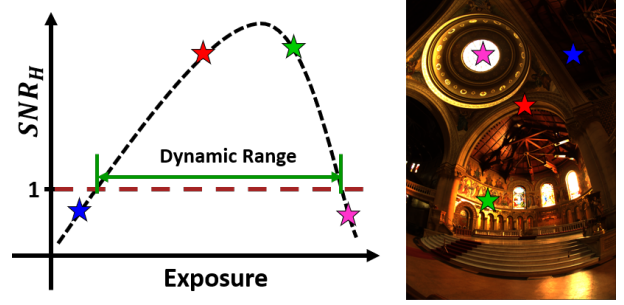


Fig. 4. **What is Dynamic Range?** Dynamic range is the range of exposure that can be detected by the sensor. We define it as the range of exposure for which SNR is greater than 1. If a particular part of a scene is darker than this range, it will appear black in the image as it becomes difficult to reconstruct it from the noise. Brighter parts of the scene will appear white as the sensor saturates outside this range. The image on the right is taken from [13].

Definition 1 (Exposure-referred SNR): Let $Y[n]$ be a pixel having an average illumination of θ photons. The exposure-referred signal-to-noise ratio SNR_H is defined as

$$\begin{aligned} \text{SNR}_H(Y[n]) &= \frac{\text{signal}}{\text{expo-ref noise}} \\ &\stackrel{\text{def}}{=} \frac{\theta}{\sigma_H} = \frac{\theta}{\sigma_Y} \frac{d\mu_Y}{d\theta} \end{aligned} \quad (8)$$

where $\mu_Y = \mathbb{E}[Y[n]]$ and $\sigma_Y = \sqrt{\text{Var}[Y[n]]}$ are the mean and standard deviation of the signal $Y[n]$, respectively, and σ_H is the exposure referred noise defined as $\sigma_H \stackrel{\text{def}}{=} \sigma_Y \frac{d\theta}{d\mu_Y}$.

There is a simple interpretation of (8). For any random quantity Y , the typical output-referred signal-to-noise ratio is $\mathbb{E}[Y]/\sqrt{\text{Var}[Y]}$. For nonlinear sensors such as QIS, we define the SNR using the exposure instead of the output so that the SNR does not “explode”. Otherwise, the truncated Poisson random variable Y will have an infinite SNR when exposure increases. Exposure-referred SNR ensures that very long exposure will have negative effects on the sensor because pixels could be saturated.

When summing a total of N independent frames that are acquired using the same integration time, we define

$$S = \sum_{n=1}^N Y[n]. \quad (9)$$

It is easy to show that the expectation and variance are

$$\mathbb{E}[S] = N\mu_Y, \quad \text{and} \quad \text{Var}[S] = N\sigma_Y^2.$$

In this case, the SNR becomes

$$\text{SNR}_H(S) = \sqrt{N} \frac{\theta}{\sigma_Y} \frac{d\mu_Y}{d\theta}. \quad (10)$$

We now present the main theoretical result. Theorem 1 shows the detailed quantities of the SNR, namely μ_Y , σ_Y and $d\mu_Y/d\theta$ for single-bit and multi-bit truncated Poisson random variables.

Theorem 1: Let $Y[n]$ be a multi-bit QIS measurement, i.e.,

$$\text{ADC}(Z_i[n]) = \begin{cases} L & \text{if } \lceil Z_i[n] \rceil \geq L, \\ Z_i[n] & \text{if } \lceil Z_i[n] \rceil < L. \end{cases}$$

Then it holds that

$$\mu_Y = \theta(\Psi_{L-1}(\theta)) + L(1 - \Psi_L(\theta)) + \Delta_\mu(\theta), \quad (11)$$

$$\sigma_Y^2 = L^2 - \sum_{q=0}^{L-1} ((2q+1)\Psi_{q+1}(\theta)) + \Delta_{\sigma^2}(\theta) - \mu_Y^2, \quad (12)$$

where $\Psi_q(\theta) = \sum_{k=0}^{q-1} \frac{\theta^k e^{-\theta}}{k!}$ is the incomplete gamma function [49], and θ is the underlying Poisson mean defined in (4)¹. The quantities $\Delta_\mu(\theta)$ and $\Delta_{\sigma^2}(\theta)$ are respectively

$$\Delta_\mu(\theta) = \sum_{k=-\infty}^{\infty} p_k \left(\sum_{q=[k]_+}^{L-1} \left(\frac{e^{-\theta}\theta^{q-k}}{(q-k)!} - \frac{e^{-\theta}\theta^q}{q!} \right) q + L(\Psi_L(\theta) - \Psi_{[L-k]_+}(\theta)) \right) \quad (13)$$

$$\Delta_{\sigma^2}(\theta) = \sum_{k=-\infty}^{\infty} p_k \left(\sum_{q=[k]_+}^{L-1} \left(\frac{e^{-\theta}\theta^{q-k}}{(q-k)!} - \frac{e^{-\theta}\theta^q}{q!} \right) q^2 + L^2(\Psi_L(\theta) - \Psi_{[L-k]_+}(\theta)) \right), \quad (14)$$

where $[\cdot]_+ = \max(\cdot, 0)$ returns the positive value, and

$$p_k = \int_{k-0.5}^{k+0.5} \frac{1}{\sqrt{2\pi\sigma_{\text{read}}^2}} e^{-\frac{x^2}{2\sigma_{\text{read}}^2}} dx \quad (15)$$

is the error probability due to read noise. The derivative $d\mu_Y/d\theta$ is

$$\begin{aligned} \frac{\partial \mu_Y}{\partial \theta} &= \Psi_{L-1}(\theta) - \theta \frac{e^{-\theta}\theta^{[L-2]_+}}{[L-2]_+!} + L \frac{e^{-\theta}\theta^{[L-1]_+}}{[L-1]_+!} \\ &+ \sum_{k=-\infty}^{\infty} p_k \left(\sum_{q=[k]_+}^{L-1} \left(-\frac{e^{-\theta}\theta^{q-k}}{(q-k)!} + \frac{e^{-\theta}\theta^q}{q!} \right) q \right. \\ &+ \sum_{q=[k]_+}^{L-2} \left(\frac{e^{-\theta}\theta^{q-k}}{(q-k)!} - \frac{e^{-\theta}\theta^q}{q!} \right) (q+1) \\ &\left. + L \left(-\frac{\theta^{(L-1)}e^{-\theta}}{(L-1)!} + \frac{\theta^{([L-k-1]_+)}e^{-\theta}}{[L-k-1]_+!} \right) \right). \quad (16) \end{aligned}$$

Proof: See supplementary document. \square

The expressions offered by Theorem 1 are dense. However, they are also *exact*. This is a generalization of the previous work by Gnanasambandam et al. [50] which showed a special case of our theorem without considering the read noise.

B. Understanding Theorem 1

To help readers gain some insights about Theorem 1, we discuss a few aspects of the theorem.

Sensor response of QIS and CIS. We first discuss the measured signal of a QIS compared to a CIS. As we discussed in the background section, a QIS pixel has a nonlinear response driven by the Poisson-Gaussian statistics, subject to an ADC. Theorem 1 shows that this signal $Y[n]$, although being random, has a mean $\mathbb{E}[Y[n]]$ given by (11):

$$\text{QIS: } \mathbb{E}[Y[n]] = \theta(\Psi_{L-1}(\theta)) + L(1 - \Psi_L(\theta)) + \Delta_\mu(\theta). \quad (17)$$

¹For notation simplicity we ignore the dark current.

We can plot this mean signal $\mathbb{E}[Y[n]]$ as a function of θ . The result is shown in Figure 5. Depending on the bit-depth of the sensor, the mean $\mathbb{E}[Y[n]]$ demonstrates a soft saturation as the exposure θ approaches the full well capacity.

In the same figure, we show the sensor response of a CIS. CIS has a linear response with respect to the exposure θ . That is,

$$\text{CIS: } \mathbb{E}[Y[n]] = \begin{cases} \theta, & \theta \leq L, \\ L, & \theta > L, \end{cases} \quad (18)$$

where L is the full well capacity of the sensor. Figure 5 shows that because of the linear response, the signal of CIS rises linearly and then saturates once it hits the full well capacity.

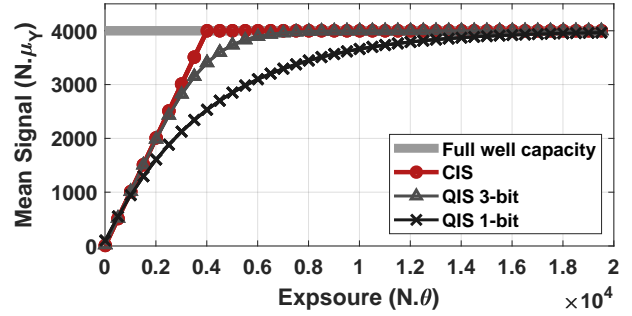


Fig. 5. **Sensor Response.** The mean signal $\mathbb{E}[Y[n]]$ of a CIS and a QIS, as a function of the exposure θ .

How SNR changes w.r.t. bit depth. Theorem 1 shows that SNR_H changes with the bit-depth. This effect is shown in Figure 6 (a). Here, we plot both the real measured QIS data and the theoretically predicted curves using different bit-depths. All curves are plotted using $N = 16$ frames. The results indicate two things: (i) The theoretical prediction matches very well the actual QIS measurement. (ii) SNR_H increases as the bit-depth increases. The latter happens because the term $\frac{d\mu_Y}{d\theta}$ drops faster for smaller bit-depth and slower for larger bit-depth. However, there is a trade-off between bit-depth and speed — 2-bit data take a much shorter time to acquire than 4-bit data.

How SNR changes w.r.t. the number of frames. Theorem 1 provides information about the number of frames. To see this, we plot the theoretically predicted curves on top of a set of real 4-bit QIS data points. Here, we use a fixed integration time Δ for all choices of N , i.e., the total exposure for $N = 4$ is $4 \times \Delta$. Figure 6 (b) shows the results. As N increases, we observe that SNR_H also increases as predicted by the \sqrt{N} term in the Theorem.

C. Dynamic range of QIS and CIS

Using Theorem 1, we compare the dynamic range of a QIS and a CIS. Recall Figure 4, the dynamic range of a sensor is defined as the range of exposure such that the SNR is above unity. Our goal here is to use the theoretical curves to predict how much dynamic range can be offered by each sensor.

Considering a typical setup of a CIS where the full-well capacity is $L = 4000 e^-$ and the read-noise is $\sigma_{\text{read}} = 2e^-$. We assume that the CIS uses three exposures to capture the

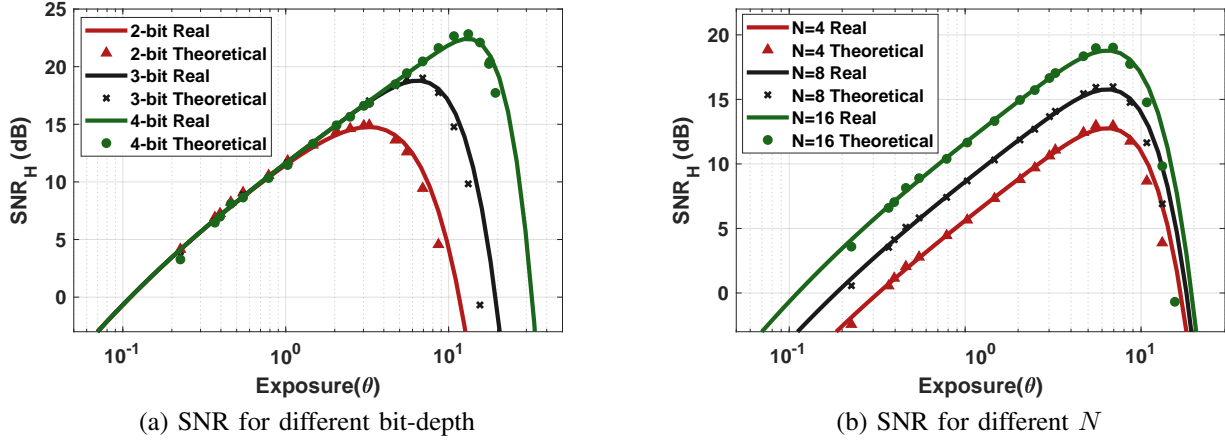


Fig. 6. **Theoretical vs Real SNR_H** (a) at different bit level. $T = 16$ frames were used to obtain all the curves. (b) with different number of frames. 4 bits data was used for obtaining all the curves. These two figures validate the correctness of Theorem 1. Notice the soft saturation of the QIS, where the SNR drops smoothly over a range of exposure levels, whereas for a CIS, there will be a sudden drop in SNR as the exposure level reaches the full-well capacity.

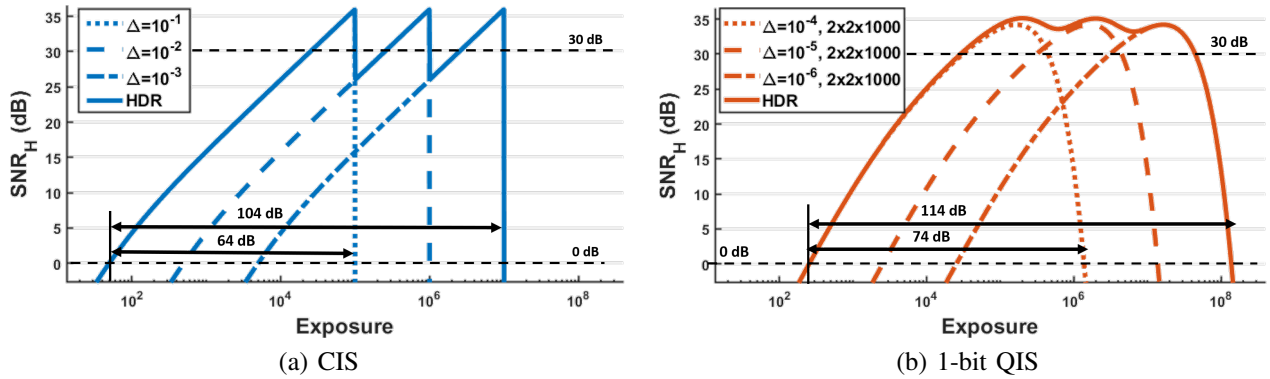


Fig. 7. **Comparison of Exposure Referred Signal-to-Noise Ratio (SNR_H) for CIS and QIS.** CIS is assumed to have a full well capacity of 4000 electrons. QIS is assumed to use a spatial oversampling of 2×2 . The number of frames at each integration time is $T = 1000$ for single-bit QIS. These oversampling is chosen such that the total signal obtained by both the CIS and QIS is the same. Notice that the QIS has a larger dynamic range than CIS for each exposure, and has a more consistent SNR over the entire range when the low dynamic range images are combined to get a single high dynamic range image.

image. For QIS, we operate in an oversampling regime by taking multiple short exposures of equal length. The number of frames is configured such that the total duration of the acquisition is the same as a CIS. Afterward, we merge the short-exposure frames to generate an HDR image using the algorithm to be described in Section IV.

Figure 7 shows the theoretically predicted curves for CIS and 1-bit QIS. For CIS, we show three different integration time $\Delta = 10^{-1}$ sec, 10^{-2} sec and 10^{-3} sec. The HDR image formed by a CIS is the sum of the three exposures. QIS with an integration time of 10^{-4} uses an oversampling of $2 \times 2 \times 1000$. This means a spatial oversampling of a 2×2 bin, and 1000 frames of 1-bit measurements. The HDR versions of the QIS data are obtained used the reconstruction method described in section IV.

As we can observe from Figure 7, the dynamic range of a QIS using just one integration time is 74dB (1-bit), which is already substantially larger than the 64dB of a CIS. After reconstructing the HDR image by merging multiple integration times, the resulting dynamic range offered by a QIS is also higher than that of a CIS. Also, Figure 7 shows that the SNR of a combined QIS image never drops below 30dB. This is a

big contrast to CIS which has a sudden drop once the exposure exceeds the full-well capacity. Figure 8 illustrates the visual comparison between a CIS and a QIS. Notice that for the same amount of photons, the QIS offers better details than a CIS.

If we look at the low light ends of Figure 7, we observe that CIS is performing better than a QIS. This phenomenon is the result of accumulating read noise from adding multiple frames. Essentially, since every readout of a QIS frame has a fixed amount of read noise, the more readouts we do the more read noise we accumulate. In Figure 9 we demonstrate this problem. Assuming a read noise level of $\sigma_{\text{read}} = 0.25$, and an integration time of $\Delta = 0.2$ sec (or $\Delta = 0.02$ sec), we plot the sum of N frames of 3-bit frames. As the number of frames N increases, with the total integration time fixed, the image becomes noisier when $\sigma_{\text{read}} = 0.25$. This is not visible, when $\sigma_{\text{read}} = 0$ or $\sigma_{\text{read}} = 0.15$, because the gaussian read noise is not strong enough to cause any issues with multiple read-outs.

D. SNR vs dynamic range trade-off

QIS offers a trade-off between the peak SNR and the dynamic range. Figure 10 shows four sets of curves: (i) a CIS running in LDR mode. The dynamic range is 64dB. (ii)

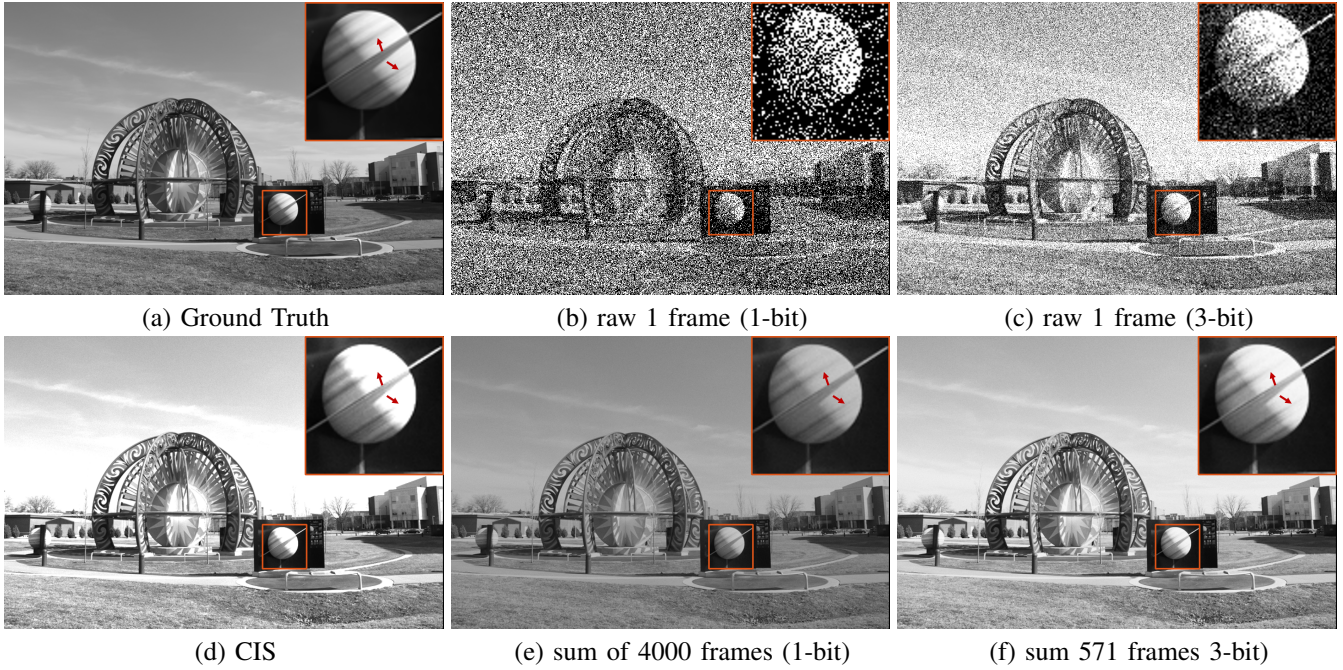


Fig. 8. **Dynamic range of QIS and CIS.** The image is simulated in such a way that the maximum illumination of the image is 6×10^6 photons per pixel per second. CIS can count up to 4000 electrons, single bit QIS - 1 electron and 3 bit QIS - 7 electrons. The exposure times are: CIS - 1ms, single bit QIS - $0.25\mu\text{s}$, and 3 bit QIS - $1.75\mu\text{s}$. We use 1 CIS frame, 4000 frames for single bit QIS and 571 frames for 3 bit QIS. In the red arrowed, we observe that CIS is saturated whereas QIS still shows the signal.

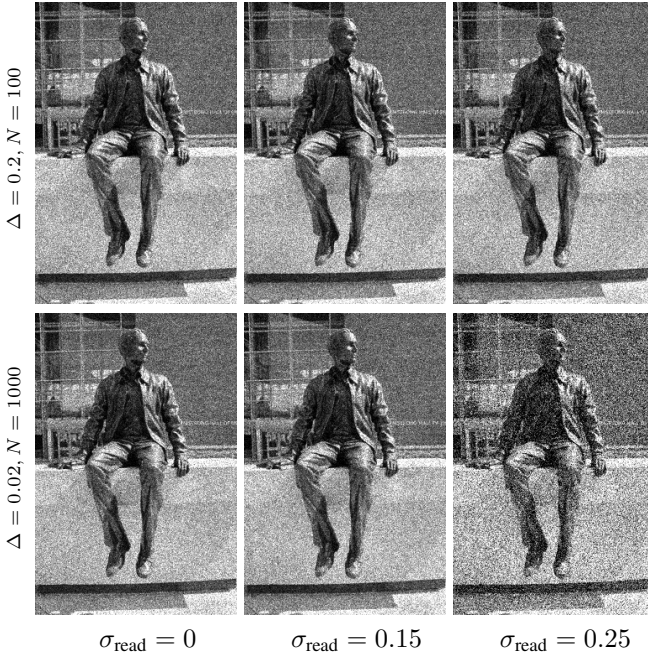


Fig. 9. **Accumulation of noise.** The sub-figures show the resulting sum of N simulated QIS frames when using different N and different integration time Δ , such the total integration time $N\Delta$ is same for all the cases considered. Because of the finite read noise, by summing more frames we accumulate error. This leads to a trade-off between the number of frames and the SNR, when the total integration time is fixed.

A QIS operating in LDR mode, with $N = 4000$ frames which is equivalent to a CIS exposure. The dynamic range is 74dB, but the peak SNR is slightly lower than that of CIS. (iii) A QIS operating in an LDR mode, with $N = 1000$ frames. This

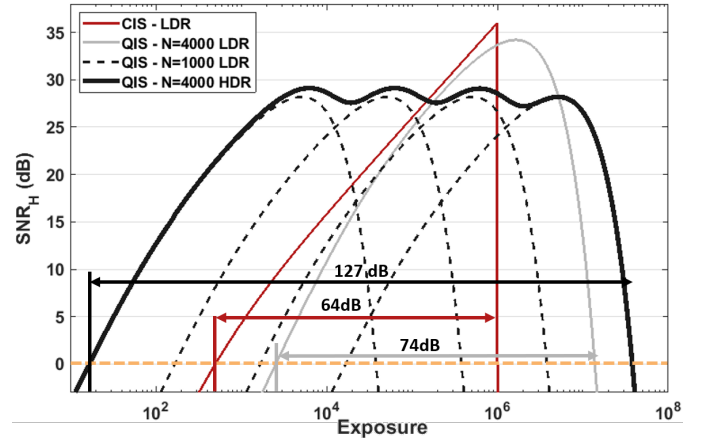


Fig. 10. **SNR vs. Dynamic Range Tradeoff.** QIS offers a unique trade-off where we can choose a setting based on whether we want an image with very high SNR or large dynamic range. In this figure, we can see that QIS can operate under an LDR regime with comparable SNR to a CIS or HDR regime, where the dynamic range is significantly higher.

is a much weaker signal than a CIS. (iv) A QIS operating in the way as the previous case, but this time we merge four different LDR images to create an HDR image. We observe that the dynamic range goes up to 127dB which is 63dB higher than that of CIS. However, because of the lower peak offered by an individual LDR, the overall peak of this HDR image is still lower than that of a CIS.

The result of this figure shows that we can trade-off the peak SNR and the dynamic range of a QIS by controlling the exposure pattern, e.g., using fewer but longer exposures, or more but shorter exposures. This flexibility can be of

importance for various imaging applications.

IV. HDR RECONSTRUCTION FOR QIS

The significance of Theorem 1 is two-fold. In the previous section, we have seen how it informs us of the SNR and hence the dynamic range of QIS. In this section, we use Theorem 1 to derive an optimal linear HDR reconstruction algorithm.

A. Exposure bracketing

Before we discuss the problem formulation, we should first comment on how a conventional CIS performs HDR reconstruction. To a large extent, conventional HDR methods are based on the concept of exposure bracketing [51]. Given a stack of differently exposed images, we construct a *linear combination* of the images to create the final image. Putting this mathematically, if we denote $\mathbf{Y}[1], \dots, \mathbf{Y}[N]$ as a sequence of N differently exposed images, then the HDR image $\hat{\lambda}$ is

$$\hat{\lambda} = \sum_{n=1}^N \mathbf{w}[n] \odot \mathbf{Y}[n], \quad (19)$$

where \odot denotes the element-wise multiplication, and $\{\mathbf{w}[n]\}$ is a sequence of weight vectors satisfying the constraint that $\sum_{n=1}^N \mathbf{w}[n] = \mathbf{1}$. Because the reconstructed image $\hat{\lambda}$ is the linear combination of the input frames, we call such an exposure bracketing technique a *linear reconstruction method*. We follow the literature by deriving the theoretical results for static scenes. We leave the methods for dynamic scenes to future work.

B. Optimal weights for QIS

Without loss of generality let us assume that the QIS has acquired a stack of frames as given by (7), where the frames are grouped into M different index sets of exposures E_1, \dots, E_M . For example, the set E_1 contains all the indices of the frames that have used the exposure Δ_1 . For simplicity, we further assume that each E_m contains K frames. So for M exposures, each having K frames, the total number of frames is $N = KM$.

To make the notation simple we focus only on one pixel. Thus, the vectorized equation can be simplified to a scalar equation. Moreover, we assume that $\lambda(t) = \lambda$ for all t so that the scene is static. Under these assumptions, the average number of photons obtained by each exposure Δ_m is

$$\theta[m] = \Delta_m \lambda, \quad (20)$$

Intuitively, since the flux λ is constant, the average number of photons is proportional to the exposure time Δ_m .

Following the QIS model, each $\theta[m]$ will generate K observations $Y[n_1], \dots, Y[n_K]$. Depending on the ADC, each $Y[n]$ can be a one-bit or a multi-bit Poisson random variable. The mean and variance of each $Y[n]$ are respectively defined as

$$\mu_Y[m] \stackrel{\text{def}}{=} \mathbb{E}[Y[n]], \quad \text{and} \quad \sigma_Y^2[m] \stackrel{\text{def}}{=} \text{Var}[Y[n]], \quad (21)$$

for $n \in E_m$, where $m = 1, \dots, M$. Essentially, this equation says that when we divide the exposures into M groups, we have M different means and variances.

Note that $\mu_Y[m]$ is a function of $\theta[m]$; $Y[n]$ is the truncated Poisson random variable according to the QIS model, and so $\mu_Y[m]$ must be a function of the underlying average photon count $\theta[m]$. Denoting $\mu_Y[m] = f(\theta[m])$ for some function f , it holds that $\theta[m] = f^{-1}(\mu_Y[m])$. For example, if the ADC is 1-bit, then

$$\mu_Y[m] = 1 - e^{-\theta[m]} \stackrel{\text{def}}{=} f(\theta[m]),$$

and so $f^{-1}(\mu_Y[m]) = -\log(1 - \mu_Y[m])$. As mentioned in [36], this can be regarded as a tone-mapping.

As far as estimation is concerned, we reconstruct a low dynamic range (LDR) image from a stack of K frames of the same exposure. We thus define the sum as

$$S[m] \stackrel{\text{def}}{=} \frac{K}{\Delta_m} f^{-1} \left(\frac{1}{K} \sum_{n \in E_m} Y[n] \right). \quad (22)$$

Here, the quantity inside f^{-1} is the average frames and f^{-1} resolves the tone-mapping. The normalization $1/\Delta_m$ ensures that $S[m]$ is properly scaled with respect to the exposure time.

To construct the HDR image, we consider using a linear combination scheme by defining

$$\hat{\lambda} = \sum_{m=1}^M w[m] S[m], \quad (23)$$

where $w[m] \in \mathbb{R}$ is a weight satisfying the property that $\sum_{m=1}^M w[m] = 1$. Because of the weighted averaging instead of a simple sum, the exposure referred SNR for this estimator $\hat{\lambda}$ takes a generalized form of (10). Specifically, since each exposure has K frames, the signal in the numerator of (10) is

$$\text{signal}^{\text{HDR}} = K\lambda.$$

The denominator of (10), which is the exposure-referred noise, becomes

$$\text{noise}^{\text{HDR}} = \sqrt{\sum_{m=1}^M \left(\frac{w[m]}{\Delta_m} \right)^2 \sigma_{\text{H}}^2[m]}, \quad (24)$$

where $\sigma_{\text{H}}[m]$ is the exposure-referred noise standard deviation of the m -th exposure ²:

$$\sigma_{\text{H}}[m] = \sqrt{K} \sigma_Y[m] \cdot \frac{d\theta[m]}{d\mu_Y[m]}. \quad (25)$$

Here, $\sigma_Y[m]$ follows from (12), and $\frac{d\theta[m]}{d\mu_Y[m]}$ follows from (14), where for each exposure m there is a different $\sigma_Y[m]$ and $\frac{d\theta[m]}{d\mu_Y[m]}$. Taking the ratio between $\text{signal}^{\text{HDR}}$ and $\text{noise}^{\text{HDR}}$ gives us the overall SNR of the HDR image:

$$\text{SNR}_{\text{H}}^{\text{HDR}} = \frac{K\lambda}{\sqrt{\sum_{m=1}^M \left(\frac{w[m]}{\Delta_m} \right)^2 \sigma_{\text{H}}^2[m]}}. \quad (26)$$

² $\sigma_{\text{H}}[m]$ can be obtained by taking the variance of $\hat{\lambda}$. The derivative appears as a result of applying the delta method to $f^{-1}(S[m])$.

The optimization problem is to find the optimal weights $w[1], \dots, w[M]$ such that $\text{SNR}_H^{\text{HDR}}$ is maximized. This gives the following constrained problem:

$$\begin{aligned} & \underset{w[1], \dots, w[M]}{\text{maximize}} && \frac{K\lambda}{\sqrt{\sum_{m=1}^M \left(\frac{w[m]}{\Delta_m}\right)^2 \sigma_H^2[m]}} \\ & \text{subject to} && \sum_{m=1}^M w[m] = 1, \text{ and } w[m] \geq 0. \end{aligned} \quad (27)$$

To specify the solution of this optimization problem, we define the m -th SNR as

$$\text{SNR}_H[m] \stackrel{\text{def}}{=} \frac{\theta[m]}{\sigma_H[m]} = \frac{\Delta_m \lambda}{\sigma_H[m]}. \quad (28)$$

With this definition, we can determine the solution.

Theorem 2: The optimal weights $w[1], \dots, w[M]$ which solves the optimization problem (27) is given by

$$w[m] = \frac{\text{SNR}_H^2[m]}{\sum_{m=1}^M \text{SNR}_H^2[m]}, \quad (29)$$

where $\text{SNR}_H[m]$ is defined by (28).

Proof: See Supplementary document. \square

C. Comparison with CIS

It is important to understand why a CIS-based reconstruction such as [12] does not work for QIS. A CIS assumes a linear sensor response until the photon level reaches the full-well capacity, whereas QIS assumes a nonlinear response. The linear response of a CIS implies that *before* saturation we have $\mu_Y[m] = \theta[m]$ so that $d\theta[m]/d\mu_Y[m] = 1$ in (25), and *after* saturation, we have that $\mu_Y[m] = L$ where L is the full-well capacity and so $d\theta[m]/d\mu_Y[m] = \infty$. For K frames, each with an exposure Δ_m , the exposure-referred SNR is

$$\begin{aligned} \sigma_H[m] &= \sqrt{K} \cdot \sigma_Y[m] \cdot \frac{d\theta[m]}{d\mu_Y[m]} \\ &= \begin{cases} \sqrt{K} \sqrt{\Delta_m \lambda}, & \text{if } \Delta_m \lambda < L, \\ \infty, & \text{if } \Delta_m \lambda \geq L. \end{cases} \end{aligned} \quad (30)$$

Substituting this into $\text{SNR}_H^{\text{HDR}}$, we show that for CIS,

$$\text{SNR}_H^{\text{HDR}} = \frac{K\lambda}{\sqrt{\sum_{m=1}^M \left(\frac{w[m]}{\Delta_m}\right)^2 K \Delta_m \lambda \cdot \mathbb{I}\{\Delta_m \lambda < L\}}}, \quad (31)$$

where $\mathbb{I}\{\cdot\} = 1$ if the argument is true, and is ∞ if the argument is false. Consequently, one can solve a similar optimization as we did to obtain the following weight

$$w[m] = \frac{\Delta_m \cdot \mathbb{I}\{\Delta_m \lambda < L\}}{\sum_{m=1}^M \Delta_m \cdot \mathbb{I}\{\Delta_m \lambda < L\}}. \quad (32)$$

Therefore, as long as the pixels are not saturated for each exposure, the weight is linear with respect to the exposure time Δ_m . This should be intuitive, because when the pixels are not saturated, longer exposure time gives higher SNR and so it should be weighted more. If a pixel becomes saturated, then the SNR will drop abruptly so that the corresponding exposure is invalidated.

The analysis here shows why a CIS-based reconstruction method does *not* apply to QIS. QIS simply does not have the linear response as CIS does. As a result, the optimal linear reconstruction method for QIS given by Theorem 2 is not transferable to CIS, and vice versa.

D. Reconstruction algorithm

Theorem 2 suggests a method to construct an HDR image. The idea is that if we knew $\text{SNR}_H[m]$, then the weight is given according to (29). Substituting the weight into (23) will give us the estimate.

In practice, however, since we do not know λ , we need to estimate $\text{SNR}_H[m]$. The estimation is based on an iterative procedure. Denoting $w^k[m]$ as the weight at the k -th iteration, and $\hat{\lambda}^k$ as the estimated HDR pixel in the k -th iteration, the iterative procedure is given by two steps:

$$\begin{aligned} \hat{\lambda}^{k+1} &= \sum_{m=1}^M w^k[m] S[m], \\ w^{k+1}[m] &= \frac{(\text{SNR}_H^{k+1}[m])^2}{\sum_{m=1}^M (\text{SNR}_H^{k+1}[m])^2}, \end{aligned}$$

where $\text{SNR}_H^{k+1}[m]$ is evaluated based on (28), and the exposure referred noise $\sigma_H[m]$, which is a function of $\hat{\lambda}$, is updated using Theorem 1. The algorithm is summarized in Algorithm 1.

Algorithm 1 HDR Image Reconstruction

1. Acquire QIS frames $Y[n]$, $n = 1, \dots, N$.
 2. Obtain M LDR images according to (22).
 3. Initialize $w^0[m] = 1/M, \forall m = 1, \dots, M$.
 4. Estimate the HDR image $\hat{\lambda}^k$ according to (23).
 5. Update $\text{SNR}_H^k[m]$ according to (28).
 6. Update weights $w^k[m]$ according to (29).
 7. Repeat 4,5,6 till convergence.
-

E. Practical considerations

Denoising. The proposed HDR reconstruction method does not include any pre-processing of the input LDR images. In practice, it may be desired to perform some degree of denoising using simple methods such as the one introduced in [36]. The denoising is particularly useful when the number of frames is low. Of course, HDR denoising itself is an open problem. There exist CIS-based denoising+HDR reconstruction methods. We leave the corresponding problem on QIS-based denoising+HDR reconstruction as future work.

Look up tables. The proposed reconstruction method depends on calculating the exposure-referred SNR for every pixel at the exposure period. This is computationally very expensive. However, we notice that the exposure-referred SNR is a function of the mean number of photons collected by the sensor at each frame. It is therefore possible to construct a look-up table to store the values by discretizing the mean signal levels. During the computation, one can just refer to the look-up table when calculating $\text{SNR}_H[m]$.

Dynamic Scenes. The optimal reconstruction scheme presented in this paper is analogous to the optimal linear schemes in the conventional CIS-based HDR problems [12], [21], [22]. Thus, by design, the method is used for static scenes. We acknowledge the importance of HDR imaging for dynamic scenes. However, in the presence of shot noise and motion, the reconstruction problem becomes substantially harder. Several methods have demonstrated the feasibility of handling photon limited data and motion, e.g., [4], [38], [52]. Adding exposure bracketing to these problems is an important future problem.

Number of iterations. The proposed reconstruction algorithm is iterative. In Figure 11, we plot the mean squared error in log scale (\mathcal{LMSE}) as used in [26] between the reconstructed image and the ground truth image after each iteration. We use the “aisle” image from the Stanford HDR image dataset [53] for simulating the QIS data for this experiment. We use three different integration times and 100 frames per integration time and use the proposed HDR reconstruction method. We observe that \mathcal{LMSE} converges after 5 iterations. We notice similar results with multiple images, different integration times and different number of frames.

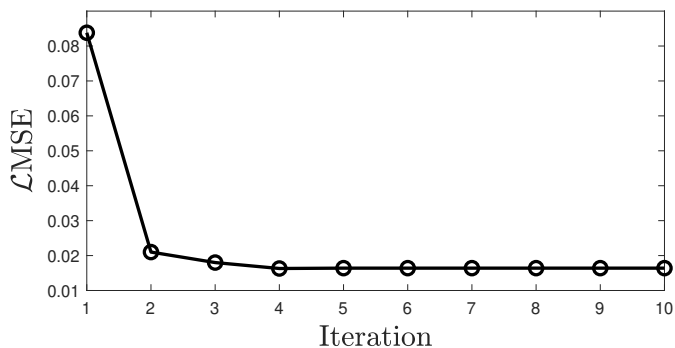


Fig. 11. Number of iterations for convergence . We use three different integration times and 100 frames per integration time and use the proposed HDR reconstruction method.. We can clearly see that \mathcal{LMSE} converges after 5 iterations.

V. EXPERIMENTS

In this section, we report the experimental results. Our results can be divided into two parts: (i) Comparing CIS with QIS for HDR imaging; (ii) Comparing the optimal HDR reconstruction algorithm and the existing methods.

A. Comparing CIS with QIS for HDR imaging

The first experiment evaluates the significance of QIS compared to CIS for HDR imaging. Some of the results have already been shown. We summarize them here:

- Figure 8 illustrates the dynamic range that can be offered by one CIS frame (in 1ms), and that offered by multiple QIS frames of different bit-depths (within the same 1ms). Our result shows that CIS saturates whereas QIS does not.
- Figure 10 shows the theoretical dynamic range of CIS and QIS. We observe that a single QIS exposure has a dynamic range of 10dB higher than that of a CIS. Fusing multiple exposures will widen the gap even further.

In addition to these results, we show in Figure 12 a visual comparison between a CIS and a QIS. This experiment considers the practical frame rate limit of a QIS, which was assumed to be 1000 frames per second according to [3]. This is approximately 30 times faster than a standard CIS operating at 30 frames per second [54]. While there exists even faster QIS prototypes (e.g., [45]), Figure 12 shows that with 1000 fps, QIS already offers an advantage over the CIS.

To conduct this experiment, we simulate 30 QIS frames for every CIS frame. The bit-depth of the QIS is 1-bit. Among the QIS exposures, we consider the multi-exposure scheme consisting of integration times 1.1 ms, 0.11 ms, and 0.011 ms. For CIS, we use integration times 33 ms, 3.3 ms, and 0.33 ms. The CIS is assumed to have a full well capacity of 4000 electrons. We use the proposed HDR reconstruction method for obtaining the QIS HDR image and [12] for the CIS HDR image. Notice that CIS produces good quality images with limited dynamic range initially, and the dynamic range improves over time. Compared to this, the QIS can produce images with a larger dynamic range at only a fraction of the time taken by the CIS to produce its first frame. Although the images are noisy initially, the quality gets better over time. At 100 ms the quality and the dynamic range of both the QIS and CIS images are about the same. But, when the total time taken reduces, QIS offers a higher dynamic range than the CIS.

In Figure 13, compare the imaging capability of QIS and CIS, using real data. We collect a total of $N = 20$ 1-bit QIS frames, with $K = 10$ frames at 2 different integration times of $50\mu s$, $1000\mu s$. We compare this to a CIS image obtained using e-con System’s e-CAM40_CUMI4682_MOD camera module which uses OmniVision’s OV4682 image sensor. Figure 13 shows a clear distinction between two sensors.

B. Reconstruction algorithm

The second experiment evaluates the optimal reconstruction scheme. While we acknowledge the promising results of deep neural network solutions, in this paper we compare with two deterministic schemes [46] and [12] for three reasons:

- The objective of this paper is not to compete with state-of-the-art HDR image reconstruction algorithms that are customized for CIS. Moreover, there does not exist QIS datasets for us to conduct a fair comparison.
- Among the deterministic methods, [12] is theoretically optimal for CIS. No other linear methods can achieve better results. We compare with this method to show that CIS methods cannot be translated to QIS.
- Among the QIS methods, [46] is one of the latest works in the literature. We compare with this method to show the effectiveness of our method.

We first evaluate the methods using the Stanford-HDR dataset [53] containing 88 HDR images. We normalize the images such that the $0.01 \leq \lambda \Delta \leq 8000$, if $\lambda \neq 0$ at every pixel. We simulate a total of $N = 3000$ 1-bit and 3-bit frames with with $K = 1000$ frames each at 3 different integration times of Δ , $\Delta/10$, and $\Delta/100$. We use the Mean Squared Error in log scale (\mathcal{LMSE}) as used in [26], PU-PSNR and PU-SSIM [55] as the metrics for comparison. \mathcal{LMSE} measures the

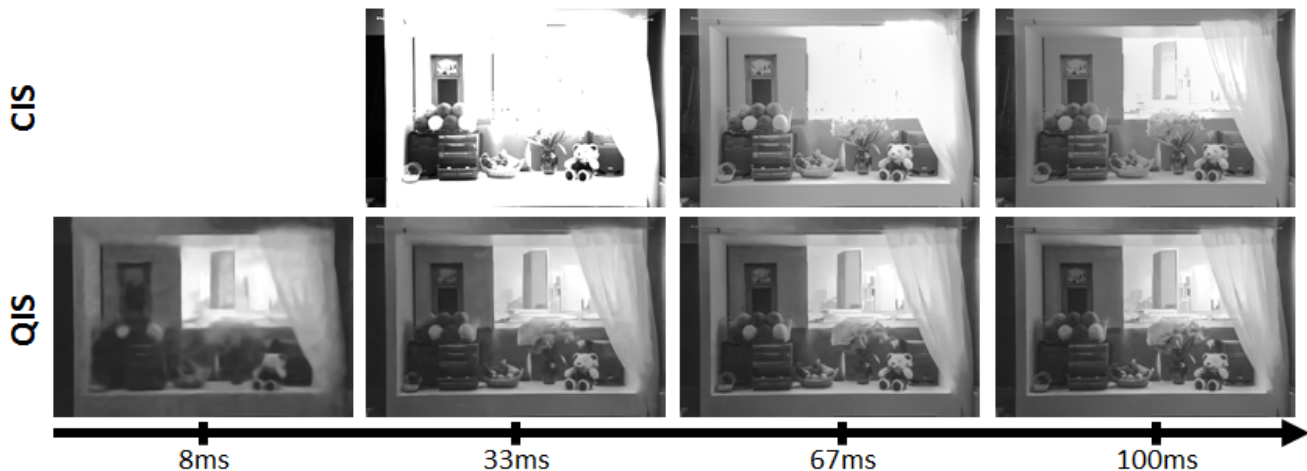


Fig. 12. **Comparing CIS and QIS for HDR imaging.** The CIS image is constructed from three frames, each with an exposure of 33 ms, 3.3 ms, and 0.33 ms, respectively. The QIS image is constructed from a set of exposures 1.1 ms, 0.11 ms, and 0.011 ms. The CIS is assumed to have a full well capacity of 4000 electrons. The number of 1-bit QIS frames is 30 times that of CIS so that the overall integration time for CIS and QIS are equal. The timestamps shown at the bottom of the figure are the overall integration time to capture all the exposures. Note that for short integration, e.g., 33ms or lower, QIS offers substantially better image reconstruction.

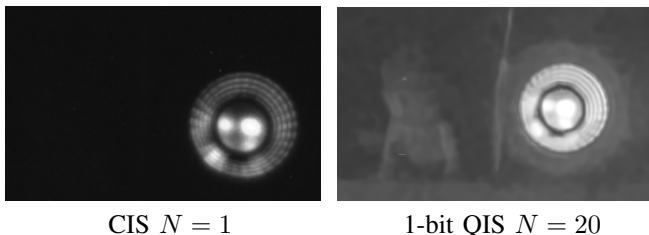


Fig. 13. **Comparing CIS and QIS.** In this real experiment, we use a commercially available CIS and compare it with a prototype QIS. Within a fixed integration time, CIS only captures one frame whereas QIS has captured multiple frames of different exposures.

Mean Squared Error (MSE) in log-scale. PU-PSNR and PU-SSIM calculate PSNR and SSIM using a perceptually uniform (PU) encoding. We compare the performance of the proposed HDR reconstruction method with reconstruction methods from [46] and [12] in Table II, using the average \mathcal{LMSE} , PU-PSNR, and PU-SSIM compared to the ground-truth for the three methods across the 88 HDR images. We can clearly see that the proposed method outperforms the two competing methods in all the three metrics that we have considered, in both single bit and three bit modes.

In Figure 14, we visually compare the three methods. We use 3-bit images. 100 frames are collected at 4 different integration times, thus giving a total of 400 frames. These frames are then used to reconstruct the high dynamic range image. Notice that the proposed method outperforms [46] and [12], both visually and the in the \mathcal{LMSE} metric.

Next, we show the comparisons using real QIS data in Figure 15. We collect a total of $N = 30$ frames of 3-bit QIS data, with $K = 10$ frames at 3 different integration times of $75\mu s$, $375\mu s$ and $1875\mu s$. The scene consists of a bright light bulb on the right and two dark objects on the left. The three LDR images show different levels of saturation. We apply [46] and [12] to the image stack and reconstruct a HDR image. We observe that the method by Dutton et al. has

a weak reconstruction of the darker regions since it provides equal weights to all the three integration times. The method by Granados et al. has better dynamic range but it also generates artifacts in the brighter regions. The proposed method, which is optimal for QIS, produces an HDR with fewer artifacts.

Finally, we show the reconstruction results for an image containing more complex content. In Figure 16, we collect a total of $N = 45$ frames, with $K = 15$ frames each at 3 different integration times of $75\mu s$, $575\mu s$ and $1175\mu s$. We use 1-bit QIS with a spatial oversampling factor of 2×2 . The denoiser from [36] used for denoising the LDR image at each integration time, before using the proposed method for HDR reconstruction. As we can observe in the images, the short exposure captures the bright regions well but the image contains noise whereas the long exposure has better SNR but saturated at bright regions. The reconstructed HDR image has recovered the details and maintained the SNR.

VI. CONCLUSION

Quanta image sensors can oversample a scene both spatially and temporally because of its ability to operate the sensor at a lower bit depth than a conventional CMOS Image Sensors. This ability, combined with lower read noise and dark current, provides QIS a unique advantage for capturing high dynamic range scenes. In this paper, we theoretically derive a closed-form expression for the signal-to-noise ratio of the QIS images. Using this result, we demonstrated the advantage of using a QIS over a CIS in terms of dynamic range and for high dynamic range imaging. We proposed a theoretically optimal high dynamic range reconstruction method. Using synthetic and real images, we demonstrated the advantage of QIS over CIS as well as the effectiveness of the proposed HDR reconstruction method.

ACKNOWLEDGEMENT

A shorter version of the paper was presented at the International Image Sensor Workshop 2019 [50]. The authors

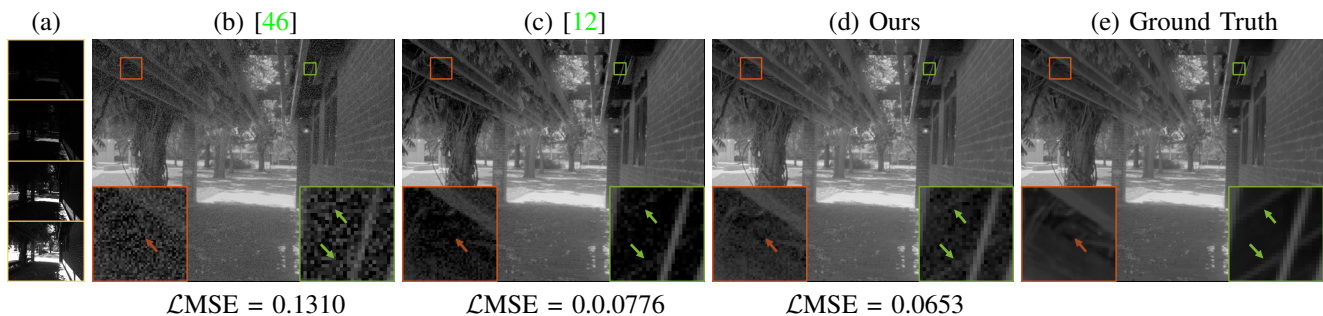


Fig. 14. **The HDR Reconstruction Algorithm - Synthetic Experiment.** A total of 400 3 bit frames were simulated at 4 different integration times, with 100 frames at each integration time. We can clearly see that the HDR images obtained in (d) using the proposed method are closer to the ground truth than the other two methods. The images are displayed on the log-scale. $\mathcal{L}MSE$ is the Mean Squared Error measure in log-scale. (Images courtesy : [53])

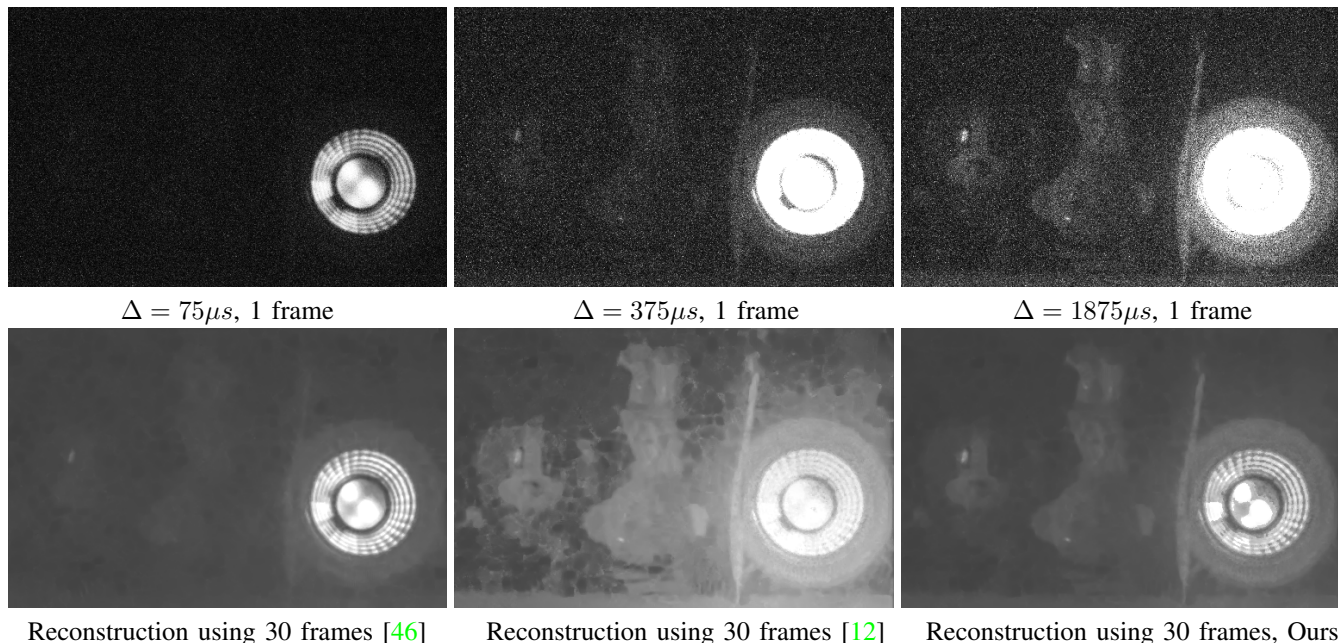


Fig. 15. **The HDR Reconstruction Algorithm - Real Experiment** In this experiment, we collect 10 QIS frames, each at 3 different exposures - $75\mu s$, $375\mu s$, and $1875\mu s$ in 3-bit modes. The result shows the advantage of the proposed HDR reconstruction methods over the other two methods.

TABLE II
COMPARING THE THREE HDR RECONSTRUCTION METHODS.

Metric	1 bit			3 bits		
	Dutton et al. [46]	Granados et al. [12]	Proposed	Dutton et al. [46]	Granados et al. [12]	Proposed
$\mathcal{L}MSE$	11.25×10^{-2}	1.23×10^{-2}	0.61×10^{-2}	10.02×10^{-2}	0.59×10^{-2}	0.49×10^{-2}
PU-PSNR	32.53	34.89	35.92	33.26	36.42	36.81
PU-SSIM	0.9138	0.9822	0.9850	0.9345	0.9901	0.9912

would like to express gratitude to Eric Fossum for providing suggestions to the IISW manuscript, and GigaJot Tech Inc. for providing the PathFinder QIS prototype camera for experiments. The work is supported, in part, by the National Science Foundation under grant CCF-1718007.

VII. APPENDIX

PROOF OF THEOREM 1

We first make the observation that

$$Y[n] = \text{ADC}(Z[n]) = \text{ADC}(\lceil Z[n] \rceil).$$

We introduce a new random variable variable $R[n] = \lceil Z[n] \rceil$. Now,

$$\begin{aligned} R[n] &= \lceil Z[n] \rceil \\ &= \lceil K[n] + \eta[n] \rceil \\ &= K[n] + \lceil \eta[n] \rceil. \end{aligned}$$

The final step is possible because $K[n]$ is an integer. We introduce another new random variable $\gamma[n] = \lceil \eta[n] \rceil$. Now the pmf of $\gamma[n]$ is

$$p_k = \mathbb{P}(\gamma[n] = k) = \int_{k-0.5}^{k+0.5} \frac{1}{\sqrt{2\pi\sigma_{\text{read}}^2}} e^{-\frac{x^2}{2\sigma_{\text{read}}^2}} dx. \quad (33)$$

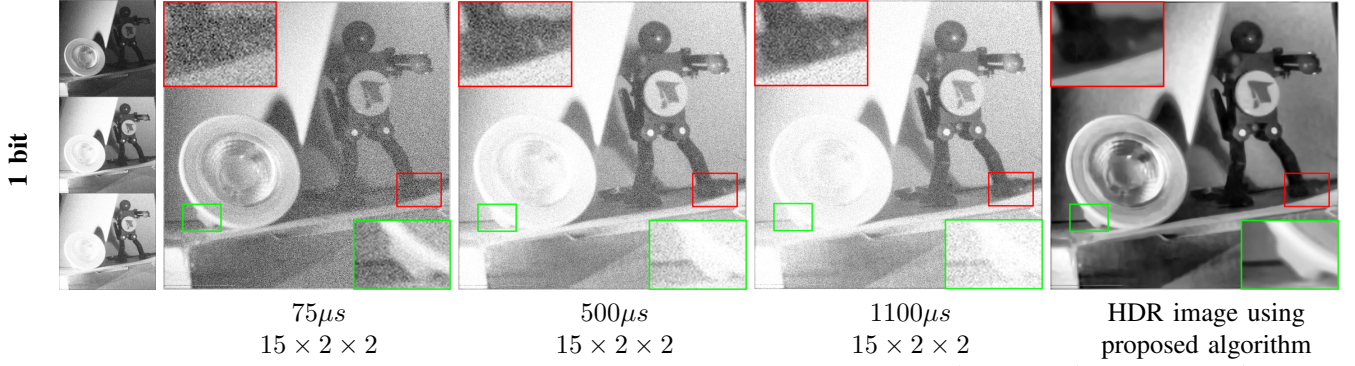


Fig. 16. **Real Experiment.** In this experiment, we obtain a $K = 15$ frames at 3 different integration times of $\Delta_1 = 75\mu s$, $\Delta_2 = 575\mu s$, and $\Delta_3 = 1175\mu s$. Spatial oversampling of 2×2 is used. The proposed HDR reconstruction algorithm is used to obtain the final HDR image. For display purpose, we use MATLAB's tonemap is re-scale the image intensity. The raw (un-normalized) images are show in the small insets on the first column.

So, $R[n] = K[n] + \gamma[n]$, where

$$\mathbb{P}(K[n] = j) = \frac{e^{-\theta}\theta^j}{j!} \text{ if } j \geq 0$$

and $\gamma[n]$ is simulated according to (33). So,

$$\mathbb{P}(R[n] = j) = \sum_{k=-\infty}^{\infty} p_k \cdot \mathbb{P}(K[n] = j - k).$$

Now, the probability mass function of $Y[n]$ is

$$\mathbb{P}(Y[n] = i) = \begin{cases} \sum_{j=-\infty}^0 \mathbb{P}(R[n] = j) & \text{if } i = 0, \\ \mathbb{P}(R[n] = i) & \text{if } 1 \leq i \leq L - 1, \\ \sum_{j=L}^{\infty} \mathbb{P}(R[n] = j) & \text{if } i = L, \\ 0 & \text{otherwise.} \end{cases}$$

Now,

$$\begin{aligned} \mathbb{E}(Y[n]) &= \sum_{q=0}^L i \cdot \mathbb{P}(Y[n] = q) \\ &= \sum_{q=1}^{L-1} q \cdot \mathbb{P}(Y[n] = q) + L \cdot \mathbb{P}(Y[n] = L) \\ &= \sum_{q=1}^{L-1} q \cdot \left(\sum_{k=-\infty}^{\infty} p_k \cdot \mathbb{P}(K[n] = q - k) \right) \\ &\quad + L \cdot \left(\sum_{q=L}^{\infty} \sum_{k=-\infty}^{\infty} p_k \cdot \mathbb{P}(K[n] = q - k) \right) \\ &= \sum_{k=-\infty}^{\infty} p_k \cdot \left(\sum_{q=1}^{L-1} q \cdot \mathbb{P}(K[n] = q - k) \right) \\ &\quad + \sum_{q=L}^{\infty} L \cdot \mathbb{P}(K[n] = q - k) \\ &= \sum_{q=1}^{L-1} q \cdot \mathbb{P}(K[n] = q) + L \cdot \sum_{q=L}^{\infty} \mathbb{P}(K[n] = q) \\ &\quad - \sum_{k=-\infty}^{\infty} p_k \cdot \left(\sum_{q=1}^{L-1} q \{ \mathbb{P}(K[n] = q - k) - \mathbb{P}(K[n] = q) \} \right) \end{aligned}$$

$$+ L \cdot \sum_{q=L}^{\infty} \{ \mathbb{P}(K[n] = q - k) - \mathbb{P}(K[n] = q) \} \quad (34)$$

In (34), $\mathbb{E}(Y[n]) = \sum_{q=1}^{L-1} q \cdot \mathbb{P}(K[n] = q) + L \cdot \sum_{q=L}^{\infty} \mathbb{P}(K[n] = q) = \mathbb{E}(K[n])$, when the read noise $\sigma_{\text{read}} = 0$. The expression corresponding to this was derived in [50] as $\theta(\Psi_{L-1}(\theta)) + L(1 - \Psi_L(\theta))$. By re-arranging the rest of the terms and utilizing the fact that $\Psi_q(\theta) = \sum_{k=0}^{q-1} \frac{\theta^k e^{-\theta}}{k!}$ and $\mathbb{P}(K[n] = j) = \frac{e^{-\theta}\theta^j}{j!}$, we can obtain the expression for $\mu_Y = \mathbb{E}(Y[n])$. We can clearly see that all the terms in (34) is differentiable. Thus, taking the derivative of (34) w.r.t. θ gives us the expression for $\frac{d\mu_Y}{d\theta}$.

The expression for σ_Y^2 can also be calculated by following similar steps as above.

PROOF OF THEOREM 2

The optimization problem is

$$\begin{aligned} &\text{maximize}_{w[1], \dots, w[M]} \frac{K\lambda}{\sqrt{\sum_{m=1}^M \left(\frac{w[m]}{\Delta_m} \right)^2 \sigma_H^2[m]}} \\ &\text{subject to} \quad \sum_{m=1}^M w[m] = 1, \text{ and } w[m] \geq 0. \end{aligned} \quad (35)$$

Using a lagrange multiplier α , we can re-write the optimization problem as

$$\min_{w[i,j]} \sum_{m=1}^M (w[m])^2 \left(\frac{\sigma_H^2[m]}{\Delta_m} \right)^2 + \alpha \left(\sum_{m=1}^M w[m] - 1 \right) \quad (36)$$

subject to $\sum_{m=1}^M w[m] = 1$, and $w[m] \geq 0$.

Solving this optimization problem, we get

$$w[m] = \frac{\left(\frac{\Delta_m}{\sigma_H[m]} \right)^2}{\sum_{k=1}^M \left(\frac{\Delta_k}{\sigma_H[k]} \right)^2}$$

Comparing this result with the expression for SNR_H , we can obtain the necessary expression.

REFERENCES

- [1] E. R. Fossum, "Some thoughts on future digital still cameras," *Image sensors and signal processing for digital still cameras*, p. 305, 2006.
- [2] E. R. Fossum, "Gigapixel digital film sensor (DFS) proposal," *Nanospace Manipulation of Photons and Electrons for Nanovision Systems*, 2005.
- [3] J. Ma, S. Masoodian, D. A. Starkey, and E. R. Fossum, "Photon-number-resolving megapixel image sensor at room temperature without avalanche gain," *OSA Optica*, vol. 4, pp. 1474–1481, Dec 2017.
- [4] I. Gyongy, N. Dutton, and R. Henderson, "Single-photon tracking for high-speed vision," *Sensors*, vol. 18, no. 2, p. 323, 2018.
- [5] A. Gnanasambandam, O. Elgandy, J. Ma, and S. H. Chan, "Megapixel photon-counting color imaging using Quanta Image Sensor," *Optics Express*, vol. 27, no. 12, pp. 17298–17310, 2019.
- [6] A. Gnanasambandam and S. H. Chan, "Image classification in the dark using Quanta Image Sensors," in *ECCV*, 2020.
- [7] Y. Chi, A. Gnanasambandam, V. Koltun, and S. H. Chan, "Dynamic low-light imaging with Quanta Image Sensors," in *ECCV*, 2020.
- [8] F. Banterle, A. Artusi, K. Debattista, and A. Chalmers, "Advanced high dynamic range imaging: Theory and practice,(2011)."
- [9] E. Reinhard, W. Heidrich, P. Debevec, S. Pattanaik, G. Ward, and K. Myszkowski, *High dynamic range imaging: acquisition, display, and image-based lighting*. Morgan Kaufmann, 2010.
- [10] T. Mitsunaga and S. K. Nayar, "Radiometric self calibration," in *CVPR*, vol. 1, pp. 374–380 Vol. 1, June 1999.
- [11] O. Gallo and P. Sen, "Stack-based algorithms for HDR capture and reconstruction," in *High Dynamic Range Video*, pp. 85–119, Elsevier, 2016.
- [12] M. Granados, B. Ajdin, M. Wand, C. Theobalt, H.-P. Seidel, and H. P. Lensch, "Optimal HDR reconstruction with linear digital cameras," in *CVPR*, pp. 215–222, 2010.
- [13] P. E. Debevec and J. Malik, "Recovering High Dynamic Range radiance maps from photographs," in *ACM SIGGRAPH 2008 classes*, p. 31, 2008.
- [14] P. Sen and C. Aguerrebere, "Practical High Dynamic Range imaging of everyday scenes: Photographing the world as we see it with our own eyes," *IEEE Signal Processing Magazine*, vol. 33, no. 5, pp. 36–44, 2016.
- [15] A. Serrano, F. Heide, D. Gutierrez, G. Wetzstein, and B. Masia, "Convolutional sparse coding for high dynamic range imaging," in *Computer Graphics Forum*, vol. 35, pp. 153–163, Wiley Online Library, 2016.
- [16] S. K. Nayar and T. Mitsunaga, "High dynamic range imaging: Spatially varying pixel exposures," in *Proceedings IEEE Conference on Computer Vision and Pattern Recognition. CVPR 2000 (Cat. No. PR00662)*, vol. 1, pp. 472–479, IEEE, 2000.
- [17] S. W. Hasinoff, D. Sharlet, R. Geiss, A. Adams, J. T. Barron, F. Kainz, J. Chen, and M. Levoy, "Burst photography for High Dynamic Range and low-light imaging on mobile cameras," *ACM Trans. Graphics (TOG)*, vol. 35, no. 6, pp. 1–12, 2016.
- [18] T. Buades, Y. Lou, J.-M. Morel, and Z. Tang, "A note on multi-image denoising," in *IEEE Intl. Workshop on Local and Non-Local Approximation in Image Processing*, pp. 1–15, 2009.
- [19] N. Joshi and M. F. Cohen, "Seeing Mt. Rainier: Lucky imaging for multi-image denoising, sharpening, and haze removal," in *ICCP*, pp. 1–8, 2010.
- [20] Y. Tsin, V. Ramesh, and T. Kanade, "Statistical calibration of CCD imaging process," in *JCCV*, vol. 1, pp. 480–487 vol.1, July 2001.
- [21] M. A. Robertson, S. Borman, and R. L. Stevenson, "Estimation-theoretic approach to dynamic range enhancement using multiple exposures," *Journal of Electronic Imaging*, vol. 12, no. 2, pp. 219–229, 2003.
- [22] K. Kirk and H. J. Andersen, "Noise characterization of weighting schemes for combination of multiple exposures;" in *BMVC 2006*, pp. 1129–1138, British Machine Vision Association, 2006.
- [23] J. Kronander, S. Gustavson, G. Bonnet, and J. Unger, "Unified hdr reconstruction from raw cfa data," in *IEEE international conference on computational photography (ICCP)*, pp. 1–9, IEEE, 2013.
- [24] S. W. Hasinoff, F. Durand, and W. T. Freeman, "Noise-optimal capture for High Dynamic Range photography," in *CVPR*, pp. 553–560, 2010.
- [25] T. Mertens, J. Kautz, and F. Van Reeth, "Exposure fusion: A simple and practical alternative to high dynamic range photography," in *Computer graphics forum*, vol. 28, pp. 161–171, Wiley Online Library, 2009.
- [26] G. Eilertsen, J. Kronander, G. Denes, R. K. Mantiuk, and J. Unger, "HDR image reconstruction from a single exposure using deep CNNs," *ACM Trans. Graphics (TOG)*, vol. 36, no. 6, pp. 1–15, 2017.
- [27] D. Marnerides, T. Bashford-Rogers, J. Hatchett, and K. Debattista, "ExpandNet: A deep convolutional neural network for High Dynamic Range expansion from Low Dynamic Range content," *Computer Graphics Forum*, vol. 37, no. 2, pp. 37–49, 2018.
- [28] N. K. Kalantari and R. Ramamoorthi, "Deep High Dynamic Range imaging of dynamic scenes," *ACM Trans. Graph.*, vol. 36, no. 4, pp. 144–1, 2017.
- [29] S. Wu, J. Xu, Y.-W. Tai, and C.-K. Tang, "Deep High Dynamic Range imaging with large foreground motions," in *ECCV*, pp. 117–132, 2018.
- [30] J.-F. Cai, H. Ji, C. Liu, and Z. Shen, "Blind motion deblurring using multiple images," *Journal of computational physics*, vol. 228, no. 14, pp. 5057–5071, 2009.
- [31] H. Zhang, D. Wipf, and Y. Zhang, "Multi-observation blind deconvolution with an adaptive sparse prior," *IEEE Trans. Pattern Analysis and Machine Intelligence*, vol. 36, no. 8, pp. 1628–1643, 2014.
- [32] M. Delbracio and G. Sapiro, "Burst deblurring: Removing camera shake through Fourier burst accumulation," in *CVPR*, pp. 2385–2393, 2015.
- [33] P. Wieschollek, M. Hirsch, B. Scholkopf, and H. Lensch, "Learning blind motion deblurring," in *JCCV*, pp. 231–240, 2017.
- [34] M. Aittala and F. Durand, "Burst image deblurring using permutation invariant Convolutional Neural Networks," in *ECCV*, pp. 731–747, 2018.
- [35] X. Tao, H. Gao, X. Shen, J. Wang, and J. Jia, "Scale-recurrent network for deep image deblurring," in *CVPR*, pp. 8174–8182, 2018.
- [36] S. H. Chan, O. A. Elgandy, and X. Wang, "Images from bits: Non-iterative image reconstruction for Quanta Image Sensors," *Sensors*, vol. 16, no. 11, p. 1961, 2016.
- [37] P. Chandramouli, S. Burri, C. Bruschini, E. Charbon, and A. Kolb, "A bit too much? High speed imaging from sparse photon counts," in *2019 ICCP*, 2019.
- [38] S. Ma, S. Gupta, A. C. Ulku, C. Brushini, E. Charbon, and M. Gupta, "Quanta burst photography," *ACM Trans. Graphics (TOG)*, vol. 39, Jul. 2020.
- [39] E. R. Fossum, "Modeling the performance of single-bit and multi-bit quanta image sensors," *IEEE Journal of the Electron Devices Society*, vol. 1, no. 9, pp. 166–174, 2013.
- [40] F. Yang, Y. M. Lu, L. Sbaiz, and M. Vetterli, "Bits from photons: Oversampled image acquisition using binary Poisson statistics," *IEEE Trans. Image Processing*, vol. 21, no. 4, pp. 1421–1436, 2011.
- [41] O. A. Elgandy and S. H. Chan, "Optimal threshold design for Quanta Image Sensor," *IEEE Trans. Computational Imaging*, vol. 4, no. 1, pp. 99–111, 2018.
- [42] E. R. Fossum, "Multi-bit Quanta Image Sensors," in *Proc. Int. Image Sensors Workshop*, pp. 292–295, 2015.
- [43] N. A. Dutton, I. Gyongy, L. Parmesan, S. Gnechi, N. Calder, B. R. Rae, S. Pellegrini, L. A. Grant, and R. K. Henderson, "A SPAD-based QVGA image sensor for single-photon counting and quanta imaging," *IEEE Trans. Electron Devices*, vol. 63, no. 1, pp. 189–196, 2015.
- [44] K. Morimoto, A. Ardelean, M.-L. Wu, A. C. Ulku, I. M. Antolovic, C. Bruschini, and E. Charbon, "Megapixel time-gated spad image sensor for 2d and 3d imaging applications," *Optica*, vol. 7, no. 4, pp. 346–354, 2020.
- [45] C. Bruschini, S. Burri, S. Lindner, A. C. Ulku, C. Zhang, I. M. Antolovic, M. Wolf, and E. Charbon, "Monolithic SPAD arrays for high-performance, time-resolved single-photon imaging," in *Intl. Conf. Optical MEMS and Nanophotonics*, pp. 1–5, IEEE, 2018.
- [46] N. Dutton, T. Al Abbas, I. Gyongy, F. Mattioli Della Rocca, and R. Henderson, "High dynamic range imaging at the quantum limit with Single Photon Avalanche Diode based image sensors," *Sensors*, vol. 18, no. 4, p. 1166, 2018.
- [47] A. Ingle, A. Velten, and M. Gupta, "High flux passive imaging with single-photon sensors," in *CVPR*, pp. 6760–6769, 2019.
- [48] J. Ma and E. R. Fossum, "Quanta Image Sensor jot with sub 0.3 e-rms read noise and photon counting capability," *IEEE Electron Device Letters*, vol. 36, no. 9, pp. 926–928, 2015.
- [49] M. Abramowitz and I. A. Stegun, *Handbook of mathematical functions with formulas, graphs, and mathematical tables*, vol. 55. US Government printing office, 1948.
- [50] A. Gnanasambandam, J. Ma, and S. H. Chan, "High Dynamic Range imaging using Quanta Image Sensors," in *Intl. Image Sensors Workshop*, 2019.
- [51] S. Mann and R. Picard, "On being undigital with digital cameras: Extending dynamic range by combining exposed pictures," in *In Proc. of IS & T 48th annual conference*, pp. 422–428.
- [52] Y. Chi, A. Gnanasambandam, V. Koltun, and S. H. Chan, "Dynamic low-light imaging with Quanta Image Sensors," in *ECCV*, 2020.

- [53] F. Xiao, J. M. DiCarlo, P. B. Catrysse, and B. A. Wandell, "High Dynamic Range imaging of natural scenes," in *Color and imaging conference*, vol. 2002, pp. 337–342, Society for Imaging Science and Technology, 2002.
- [54] B. McLernon, *Canon EOS 5D Mark II Digital Field Guide*, vol. 204. John Wiley & Sons, 2012.
- [55] T. O. Aydın, R. Mantiuk, and H.-P. Seidel, "Extending quality metrics to full luminance range images," in *Human vision and electronic imaging xiii*, vol. 6806, p. 68060B, International Society for Optics and Photonics, 2008.